Published in final edited form as:
Science. 2017 December 22; 358(6370): 1622–1626. doi:10.1126/science.aao4277.

Spatial reconstruction of immune niches by combining photoactivatable reporters and scRNA-seq

Chiara Medaglia[#1], **Amir Giladi**[#1], **Liat Stoler-Barak**[#1], **Marco De Giovanni**[#2], **Tomer Meir Salame**[3], **Adi Biram**[1], **Eyal David**[1], **Hanjie Li**[1], **Matteo Iannacone**[#2,‡], **Ziv Shulman**[#1,‡], **Ido Amit**[#1,‡]

[1]Department of Immunology, Weizmann Institute of Science, Rehovot, Israel

[2]Division of Immunology, Transplantation and Infectious Diseases and Experimental Imaging Center, IRCCS (Istituto di Ricovero e Cura a Carattere Scientifico) San Raffaele Scientific Institute and Vita-Salute San Raffaele University, Milan 20132, Italy

[3]Flow Cytometry Unit, Department of Biological Services, Weizmann Institute of Science, Rehovot, Israel

[#] These authors contributed equally to this work.

Abstract

Cellular functions are strongly dependent on surrounding cells and environmental factors. Current technologies are limited in their ability to characterize the spatial location and gene programs of cells in poorly structured and dynamic niches. We developed a method, NICHE-seq, that combines photoactivatable fluorescent reporters, two-photon microscopy, and single-cell RNA sequencing (scRNA-seq) to infer the cellular and molecular composition of niches. We applied NICHE-seq to examine the high-order assembly of immune cell networks. NICHE-seq is highly reproducible in spatial tissue reconstruction, enabling identification of rare niche-specific immune subpopulations and gene programs, including natural killer cells within infected B cell follicles and distinct myeloid states in the spleen and tumor. This study establishes NICHE-seq as a broadly applicable method for elucidating high-order spatial organization of cell types and their molecular pathways.

Immune function depends on the dynamic interactions of heterogeneous cell types with the tissue microenvironment. Both innate and adaptive immune responses rely on signals from neighboring cells to initiate cell fate decisions and deploy effective defensive, metabolic, or tissue repair programs. For example, macrophages exhibit specialized organ-specific cellular functions owing to interactions with distinct cells in different tissues (1). Spatial heterogeneity in immune niches has typically been studied by microscopy-based methods (2–4). These have allowed the identification of important immune functions that are dependent on the spatial location of various tissue-resident immune cells and environmental factors (5, 6). Despite this important progress, most of these findings remain anecdotal, because we still lack a systematic approach to characterize the cellular compositions and molecular pathways of functional tissue niches.

[‡]**Corresponding author.** iannacone.matteo@hsr.it (M.I.); ziv.shulman@weizmann.ac.il (Z.S.); ido.amit@weizmann.ac.il (I.A.).

Europe PMC Funders Author Manuscripts

Single-cell RNA sequencing (scRNA-seq) is emerging as an important tool to study the functional space of immune cell types and states (7, 8). Currently, most scRNA-seq techniques require tissue homogenization, with the inevitable loss of spatial information (9). Further, because mammalian tissues are composed of trillions of cells that reside in specific tissue subcompartments and whose relative abundances vary by several orders of magnitude, brute force approaches may not be effective in identifying rare populations of cells congregated in a particular niche (10). Techniques combining scRNA-seq with spatial information obtained through various barcoding approaches show promising results but are limited in sequencing depth and widespread utility (11–14). Similarly, methods for spatial reconstruction of tissue that combine scRNA-seq with single-molecule fluorescence in situ hybridization of a few “landmark genes” are effective, but they depend on structured tissue organizations and a priori knowledge of differentially expressed genes and are therefore limited in their applicability (15, 16).

To overcome these limitations, we developed NICHE-seq, a method that combines photoactivatable fluorescent markers, two-photon laser scanning microscopy (TPLSM), and flow cytometry–based fluorescence-activated cell sorting (FACS) coupled to massively parallel scRNA-seq [MARS-seq (7)]. We used transgenic mice ubiquitously expressing a photoactivatable green fluorescent protein (PA-GFP) that allows precise in situ labeling by two-photon irradiation of diverse cellular niches in both live animals and ex vivo settings (6). After tissue dissociation, niche-specific labeled cells can be analyzed by MARS-seq, thus combining transcriptional cell state and spatial information (fig. S1).

To visualize specific tissue niches, we intravenously transferred 2×10^7 TdTomato$^+$ T cells and 4×10^7 CFP$^+$ B cells into PA-GFP mice to serve as landmark cells and photoactivated the B cell follicles or the T cell area of inguinal lymph nodes (LNs) at 820 nm. Subsequent imaging at 940 nm confirmed the bright and specific activated PA-GFP signal only within the photoactivated areas (Fig. 1A). To further examine the cell-labeling specificity, we analyzed by FACS the frequency of PA-GFP$^+$ cells in photoactivated and nonphotoactivated (control) LNs from the same mice. We observed specific activated PA-GFP$^+$ cells in photoactivated LNs, with no labeled cells in control LNs not subjected to photoactivation (fig. S2A). FACS analysis of the photoactivated B cell follicles showed that activated PA-GFP$^+$ cells constituted 1.5% of the total live cells. Of these, 92% were B cells and 8% were T cells (6.7% CD4$^+$ and 1.3% CD8$^+$) (Fig. 1B and fig. S2A). Analysis of photoactivated cells from the T cell area showed similar specificity: Of the activated PAGFP$^+$ cells, 90%were T cells (37%CD4$^+$ and 53% CD8$^+$) and 10%were B cells (Fig. 1B and fig. S2A).

To evaluate the effectiveness of niche photoactivation with single-cell genomic profiling for spatial reconstruction, we performed MARS-seq analysis on sorted, photoactivated cells (fig. S1, B to F). Clustering analysis (17) of 3900 photoactivated cells from B cell follicles and T cell areas identified five major clusters including B cells, CD4$^+$ T cells, and CD8$^+$ T cells (Fig. 1C; fig. S2, B to D; and table S1). Overlaying the niche labels on top of the clusters showed results comparable to the FACS analysis, with 39% of the PA-GFP$^+$ cells from the T cell area corresponding to CD4$^+$ and 56% to CD8$^+$ T cell subsets (Fig. 1C). Similarly, within B cell follicles, 95% of the cells corresponded to B cells. To evaluate the enrichment of cells in a particular niche de novo, we sequenced an additional 487 cells from a control LN that

was not photoactivated and calculated the enrichment of the same cell types and states in the PA-GFP$^+$ niche as compared with data from random single-cell sampling of the entire tissue (Fig. 1D) (17). This analysis showed more than twofold enrichment of B cells and depletion of CD4$^+$ and CD8$^+$ T cells in the B cell follicles compared with the entire LN (Fig. 1D). Similarly, in the T cell area, B cells were depleted, whereas CD4$^+$ and CD8$^+$ T cells were enriched (Fig. 1D). These results were highly reproducible across biological replicates of photoactivated LNs from different mice (fig. S2E). Importantly, photoactivation did not induce notable changes in gene expression; photoactivated and control T or B cells showed similar gene expression profiles (fig. S2F).

Under homeostatic conditions, and especially during immune challenges, the B and T cell regions in LNs host rare populations of cells from different lineages that fulfill various critical functions, such as antigen presentation and costimulation. To evaluate the sensitivity of NICHE-seq in identifying and characterizing these populations, we injected lymphocytic choriomeningitis virus (LCMV) into the footpad of PA-GFP mice and applied NICHE-seq to measure the change in the cellular composition of the B cell follicles and T cell areas in inguinal LNs 72 hours after infection (fig. S3, A and B). Clustering of 8100 cells identified seven major cell types, including B cells, CD4$^+$ T cells, CD8$^+$ T cells, natural killer (NK) cells, dendritic cells (DCs), and inflammatory monocytes (Fig. 1E; fig. S3, C to E; and table S2). Monocytes and DCs were predominantly localized in the T cell area and enriched within this area compared with the B cell follicle or the total LN (Fig. 1, E and F, and fig. S3F), which is consistent with previously published data (4). The inflammatory monocyte subset enriched within the T cell area expressed many cell type–specific genes associated with antiviral pathways, including *Ifi204*, *Cxcl10*, and *Cxcl9* (18) (fig. S3,G and H). These results were reproducible across different experiments and animals (fig. S3I). Together, our data confirm the reproducibility, sensitivity, and specificity of the NICHE-seq technology in characterizing specific niches within LNs, including rare subpopulations, both at steady state and upon viral infection.

We next sought to extend the NICHE-seq approach to the spleen. To identify the composition of the splenic B cell follicles, T cell areas, and the marginal zone (MZ, or the interface between the nonlymphoid red pulp and the lymphoid white pulp), we used three different cellular landmarks. Fluorescently labeled B and T cells were adoptively transferred into irradiated wild-type mice previously transplanted with bone marrow cells from PA-GFP and CX_3CR1-GFP mice (at a 7:3 ratio). We sorted and sequenced 7852 photoactivated PA-GFP$^+$ single cells from these niches (Fig. 2, A and B; fig. S4A; and table S3). We found a high degree of heterogeneity, with 16 different clusters (Fig. 2B and fig. S4, B to D). These included several subsets of B and T cells, as well as myeloid cells, plasma cells (PCs), and NK cells. Sequencing 3071 immune cells from the total spleen for reference, we found that many of the different cell types are highly specific to particular niches (fig. S4E). For example, regulatory T cells (T_{regs}) were specifically localized to the T cell area and defined by high expression of *Foxp3*, *Cd4*, *Icos*, and *Folr4* (Fig. 2, C and D). The MZ niche displayed high complexity with various myeloid cell types, including a MZ macrophage population expressing high levels of *Vcam1*, *Hmox1*, *C1qb*, and *Cd5l* (Fig. 2, B to D). Immunofluorescence histology further confirmed the specific localization of these

VCAM-1^{+} CD5L^{+} macrophages in the MZ (fig. S5). As before, these nichespecific cell networks were reproducibly identified across biological replicates (Fig. 2C and fig. S4F).

To further characterize the dynamics of splenic niches upon systemic viral infection, we intravenously injected PA-GFP mice with LCMV 48 hours before photoactivation and NICHE-seq analysis. Globally comparing the transcriptional changes of 15,452 cells in different splenic regions—MZ, T cell area, and B cell follicles—we observed substantial changes in the representation of cell types within specific tissue niches, which were reproducibly identified across biological replicates (fig. S6, A and B). To better define the dynamics of each cell population in these regions, we measured the changes in the frequencies of all cell populations in every niche before and after infection (Fig. 3A and fig. S6C). We found nichespecific and cell-specific changes. For example, after infection, the number of NK cells was significantly increased in B cell follicles but decreased in the MZ (Fig. 3A). These changes in the localization of NK cells upon LCMV infection were confirmed by confocal immunofluorescent histology (Fig. 3, B and C).

LCMV replicates in specific structures and cell types in the spleen (19), but the cellular and molecular composition of the LCMV-infected niche is not fully understood and is difficult to study with current technologies. We used a recombinant LCMV strain that selectively drives GFP expression within infected cells (4) to identify and photoactivate the LCMV-replicating niche, which includes the cells interacting with the infected area (fig. S7A). Comparing the virusreplicating area with the total infected spleen, we found that the former was enriched with NK cells, monocytes, and macrophages (Fig. 3D). Single-cell analysis can indicate the proliferative potential of each cell (20); measuring the percent of proliferating cells, we found that NK cells, induced T_{regs}, and PCs were more proliferative in the LCMV-infected area than in the total infected spleen (fig. S7, B to D). The distinct expression signatures of immune cells within the infected niche compared with those of the same cell types in other regions are poorly understood. Comparing the transcriptional state of each cell type in the total infected spleen versus in the LCMV-infected area, we observed niche-specific expression programs (Fig. 3E and fig. S7E). For example, monocytes in the infected area, but not in other locations in the spleen, up-regulated the T cell chemoattractant *Cxcl9*, which attracted leukocytes expressing its receptor CXCR3 (Fig. 3E). In contrast, regulators of inflammatory response (e.g., *Trem3*) were expressed at higher levels in monocytes outside the infected area and in much lower levels within the infected area (Fig. 3E). These niche-specific cell assemblies were reproducibly identified across biological replicates (fig. S6B).

Although single-cell genomic analyses are already extending our knowledge to previously unexplored cell types and gene pathways, dissecting the cellular networks in tissues and organs imposes a major challenge. Our newly developed NICHE-seq technology is a robust and flexible approach for characterizing and modeling the cross-talk between various immune cell types and the local microenvironment and is applicable in different biological systems. For example, applying NICHE-seq to measure the immune composition of various niches in B16.F10 melanoma tumors, we identified different myeloid compositions within niches that have different extracellular matrix structures (fig. S1 and fig. S8, A and B). Inflammatory monocytes (CCR2^{high}/Ly6C^{high}) were localized in regions of straight collagen fibers, whereas tumor-associated macrophages were localized in less organized, curly

collagen fibers regions (fig. S8, C and E). Critically, understanding how multicellular organisms assemble high-order functional units through communication between different cell types in support of shared goals, such as the function of the immune system, may pave the way to engineering tissue function, with important potential for future development of immunotherapeutic strategies.

Our experiments also highlight several opportunities for improvement. First, increasing the palette of photoactivatable fluorescent reporters beyond PA-GFP would improve the spatial resolution and throughput. This could be also achieved by introducing various fate mapping and optogenetic techniques for combined analysis of regional functions and transcriptomes. Second, the excitation is currently binary (on/off), whereas a gradient form of activation intensity and additional photoactivatable reporters combined with index sorting could generate finer resolution of cell organization within the labeled niche (8). Third, the analytical challenges of identifying the cell assemblies and correctly modeling these niches will require the development of algorithms that can accurately analyze the coexistence of overlapping transcriptional programs and successfully ameliorate the types of biases produced by comparing highly different cellular niches. Fourth, the current version of NICHE-seq is limited to genetically engineered model organisms, but antibody-conjugated photoactivatable dyes could be developed for human NICHE-seq studies. Despite the current limitations, our proof-of-principle study shows that NICHE-seq can be used as a molecular microscope that adds the spatial dimension to single-cell genomic data, enabling comprehensive investigation of a large number of tissue structures at single-cell resolution.

Supplementary Material

Refer to Web version on PubMed Central for supplementary material.

Acknowledgments

I.A. is supported by the Chan Zuckerberg Initiative; the Howard Hughes Medical Institute International Scholar Award; European Research Council Consolidator Grant 724471-HemTree2.0; a Melanoma Research Alliance Established Investigator Award (509044); the Israel Science Foundation (703/15); the Ernest and Bonnie Beutler Research Program of Excellence in Genomic Medicine; the Helen and Martin Kimmel Award for Innovative Investigation; a Minerva Stiftung research grant; the Israeli Ministry of Science, Technology, and Space; the David and Fela Shapell Family Foundation; the NeuroMac DFG (German Research Foundation)/Transregional Collaborative Research Center Grant; and the Abramson Family Center for Young Scientists. Z.S. is supported by European Research Council grant 677713, the Morris Kahn Institute for Human Immunology and Human Frontiers of Science Program (CDA-00023/2016), the Azrieli Foundation, the Rising Tide Foundation, grants from the Benoziyo Endowment Fund for the Advancement of Science, the Sir Charles Clore Research Prize, the Comisaroff Family Trust, the Irma and Jacques Ber-Lehmsdorf Foundation, the Gerald O. Mann Charitable Foundation, and the David M. Polen Charitable Trust. M.I. is supported by European Research Council Consolidator Grant 725038, Italian Association for Cancer Research grant 15350, Italian Ministry of Health grant GR-2011-02347925, Fondazione Regionale per la Ricerca Biomedica grant 2015-0010, the European Molecular Biology Organization Young Investigator Program, and a Career Development Award from the Giovanni Armenise-Harvard Foundation. A.G. is a recipient of the Clore Fellowship. H.L. is funded by a Marie Curie Individual Fellowship (European Union project 746382, SCALTIE). The data reported in this manuscript are presented in the main paper and the supplementary materials. Raw and processed scRNA-seq data have been deposited in the National Center for Biotechnology Information Gene Expression Omnibus with accession number GSE104054.

References

1. Lavin Y, et al. Cell. 2014; 159:1312–1326. [PubMed: 25480296]
2. Shulman Z, et al. Science. 2014; 345:1058–1062. [PubMed: 25170154]

3. Guidotti LG, et al. Cell. 2015; 161:486–500. [PubMed: 25892224]
4. Sammicheli S, et al. Sci Immunol. 2016; 1:eaah6789. [PubMed: 27868108]
5. Qi H, Kastenmüller W, Germain RN. Annu Rev Cell Dev Biol. 2014; 30:141–167. [PubMed: 25150013]
6. Victora GD, et al. Cell. 2010; 143:592–605. [PubMed: 21074050]
7. Jaitin DA, et al. Science. 2014; 343:776–779. [PubMed: 24531970]
8. Paul F, et al. Cell. 2015; 163:1663–1677. [PubMed: 26627738]
9. Stegle O, Teichmann SA, Marioni JC. Nat Rev Genet. 2015; 16:133–145. [PubMed: 25628217]
10. Pollen AA, et al. Nat Biotechnol. 2014; 32:1053–1058. [PubMed: 25086649]
11. Lovatt D, et al. Nat Methods. 2014; 11:190–196. [PubMed: 24412976]
12. Raj A, van Oudenaarden A. Annu Rev Biophys. 2009; 38:255–270. [PubMed: 19416069]
13. Ståhl PL, et al. Science. 2016; 353:78–82. [PubMed: 27365449]
14. Shaffer SM, et al. Nature. 2017; 546:431–435. [PubMed: 28607484]
15. Satija R, Farrell JA, Gennert D, Schier AF, Regev A. Nat Biotechnol. 2015; 33:495–502. [PubMed: 25867923]
16. Shah S, Lubeck E, Zhou W, Cai L. Neuron. 2017; 94:752–758.e1. [PubMed: 28521130]
17. Materials and methods are available as supplementary materials.
18. Eickhoff S, et al. Cell. 2015; 162:1322–1337. [PubMed: 26296422]
19. Duhan V, et al. Sci Rep. 2016; 6
20. Scialdone A, et al. Methods. 2015; 85:54–61. [PubMed: 26142758]

Europe PMC Funders Author Manuscripts

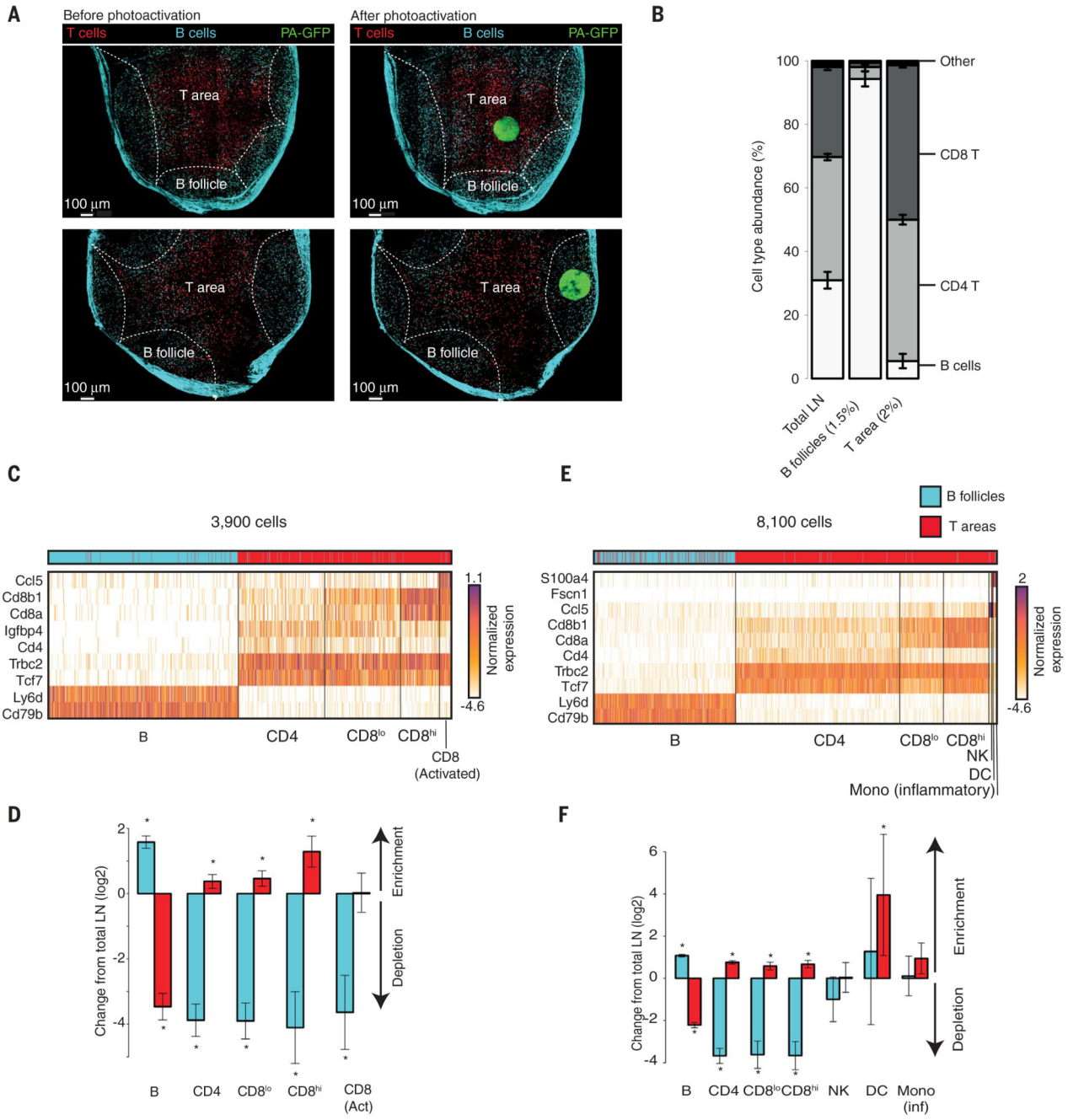

Fig. 1. NICHE-seq accurately and reproducibly depicts the cellular composition of defined niches.

(**A**) TPLSM images of naive inguinal lymph nodes (LNs) from PA-GFP host mice, before and after photoactivation of subregions (green). Adoptively transferred TdTomato^{+} cells (red) and CFP^{+} B cells (cyan) mark the T cell area and the B follicles, respectively. Second harmonic generation was used to detect collagen fibers (cyan). (**B**) Cell type distribution in the unlabeled LN and photoactivated B cell follicles and Tcell areas, measured by flow cytometry. Error bars represent standard error from three independent experiments. (**C**) Gene

expression profiles of 3900 single cells from photoactivated B cell follicles or Tcell areas of naive inguinal LNs, grouped into five clusters (table S1). The color bar at the top indicates each cell's origin. Expression is normalized by total cell count and highest gene value. (**D**) Relative enrichment of different cell types in each subregion ($\log_2$ fold change compared with the total naive LN). Error bars represent 90% confidence intervals. *$q < 0.001$; Fisher test. (**E**) Same as (C), but for 8100 single cells from inguinal LNs, 72 hours after infection with LCMV, grouped into seven clusters (table S2). Mono, monocytes; act, activated; inf, inflammatory. (**F**) Same as (D), but for LCMV-infected cells.

Europe PMC Funders Author Manuscripts

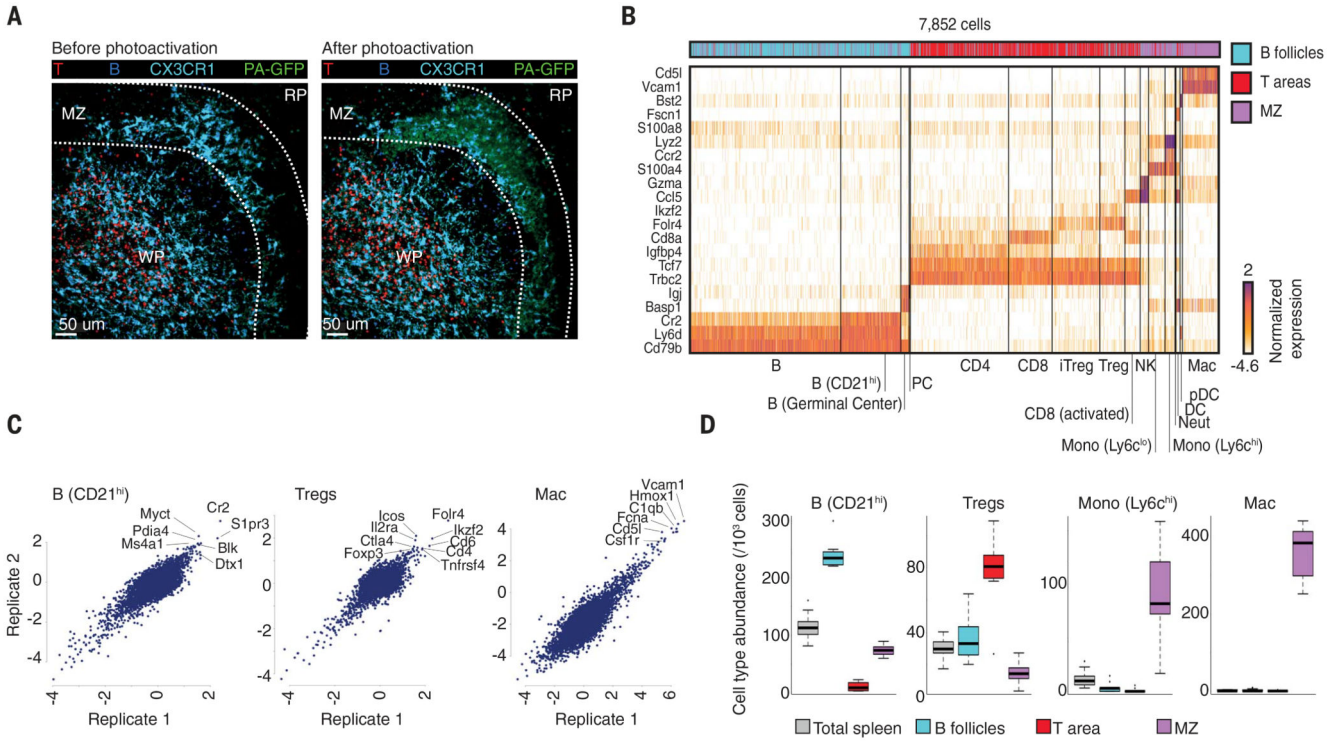

Fig. 2. Characterization of the cellular composition of diverse splenic niches.

(**A**) TPLSM images of naive spleens of PA-GFP/CX_3CR1-GFP chimeric mice (17), showing CX_3CR1^+ cells (cyan), T cell areas labeled with adoptively transferred $DsRed^+$ T cells (red), and B cell follicles labeled with CFP^+ B cells (blue), before and after photoactivation of the MZ (green). WP, white pulp; RP, red pulp. Results represent three independent experiments. (**B**) Gene expression profiles of 7852 single cells from photoactivated splenic B cell follicles, Tcell areas, or MZs, grouped into 16 clusters (table S3). The color bar at the top indicates each cell's origin. iT_{reg}, induced T_{regs}; neut, neutrophils, pDC, plasmacytoid DCs; mac, macrophages. (**C**) Relative gene expression in different cell types (log_2 fold change compared with expression in other detected splenic cell types). The *x* and *y* axes represent relative expression in two biological replicates. (**D**) Relative abundances of different cell types in splenic niches and the total spleen. Data represent cell counts from both biological and technical replicates (fig. S1, B to F). Cell counts were divided by the total number of cells and multiplied by 1000.

Europe PMC Funders Author Manuscripts

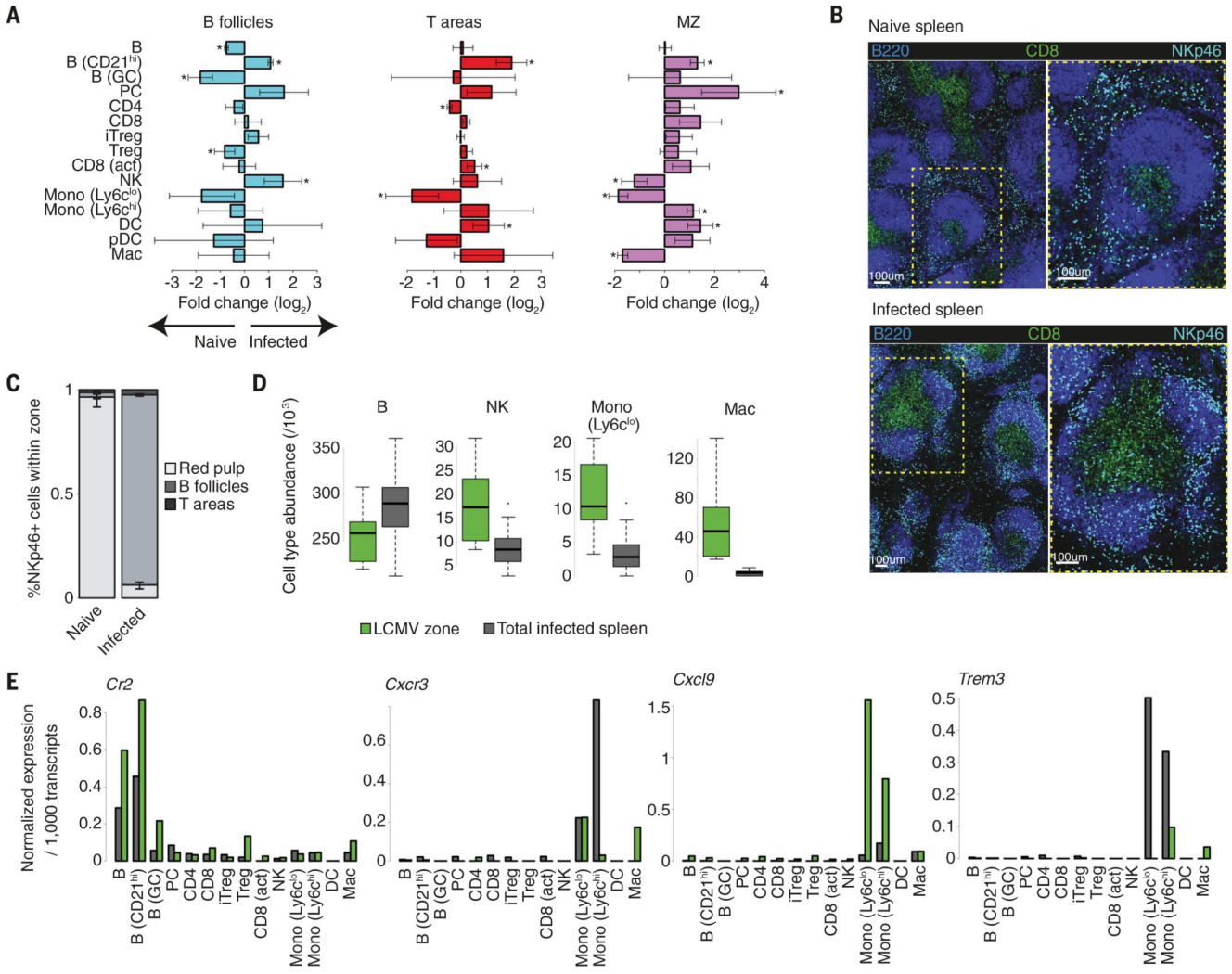

Fig. 3. Viral infection induces distinct changes in the cellular and molecular composition of specific splenic niches.

(**A**) Changes in splenic B cell follicle, T cell area, and MZ cellular compositions upon LCMV infection compared with their naive equivalents. Error bars represent 90% confidence intervals. *$q < 0.001$; Fisher test. (**B**) Representative confocal images from NKp46iCre x Rosa26 TdTomato reporter mice showing tissue localization of NKp46$^+$ NK cells (cyan) in naive and LCMV-infected spleens. B220$^+$ cells (blue) and CD8$^+$ cells (green) mark B cell follicles and T cell areas, respectively. These data are representative of two independent experiments. (**C**) Quantification of NKp46$^+$ cells in B cell follicles and red pulp in two replicates. Error bars represent the range between two experiments. (**D**) Relative abundances of different cell types in the LCMV-replicating area and the total LCMV-infected spleen. Data represent cell counts from both biological and technical replicates (fig. S1, B to F). Cell counts were divided by the total number of cells and multiplied by 1000. (**E**) Mean expression levels of genes showing significant cell type–specific differences between the LCMV-replicating area and the total LCMV-infected spleen ($q < 0.001$; χ^2 test).

Europe PMC Funders Author Manuscripts

Bars indicate the average unique molecular identifier count per 1000 transcripts, normalized to cell size.

Europe PMC Funders Author Manuscripts